metals

MDPI

Article

Microstructural Insights into Solid Particle Erosion in a High-Chromium Cast Iron

Alessio Suman, Annalisa Fortini * and Nicola Zanini

Department of Engineering, University of Ferrara, 44122 Ferrara, Italy; alessio.suman@unife.it (A.S.); nicola.zanini@unife.it (N.Z.)

* Correspondence: annalisa.fortini@unife.it

Abstract: Solid particle erosion (SPE) significantly limits the service life of High-Chromium Cast Irons (HCCIs), widely used in power generation and mining industries. This study investigates how microstructural features influence the erosion resistance of a Fe-Cr-C cast iron, focusing on the interplay between particle kinetic energy and carbide features, i.e., carbide volume fraction (CVF). Erosion tests, conducted per ASTM G76 standards, revealed that substrates with similar CVFs exhibited varying damage levels, even at consistent particle kinetic energies. The findings underscored that impact conditions have a greater influence on erosion resistance than CVF alone, emphasizing the critical role of carbide morphology and distribution in mitigating damage. This work provides valuable insights for optimizing HCCIs to enhance material performance and durability in demanding erosive environments by tailoring carbide distribution to specific operational conditions.

Keywords: high-chromium cast irons; solid particle erosion; carbide volume fraction; impact velocity; image analysis; erosion rate

Academic Editor: Qinghuan Huo

Received: 25 November 2024
Revised: 23 December 2024
Accepted: 24 December 2024
Published: 26 December 2024

Citation: Suman, A.; Fortini, A.; Zanini, N. Microstructural Insights into Solid Particle Erosion in a High-Chromium Cast Iron. *Metals* **2025**, *15*, 6. https://doi.org/10.3390/met15010006

1. Introduction

Solid particle erosion (SPE) is a widely studied phenomenon in the engineering field, characterized by material removal resulting from impacting particles [1–5]. This process poses significant challenges in applications such as gas turbines, slurry pumps, and heat exchangers, where repeated solid particle impacts cause mass loss, compromising durability and reliability [6–10]. Addressing erosion-related issues is crucial for extending the service life of these components and maintaining overall efficiency and safety. SPE is a complex, multi-faceted phenomenon influenced by a combination of parameters that determine the severity and nature of surface degradation. The literature extensively discusses these parameters, which include the carrying fluid (such as kinetic energy and thermodynamic states), the material properties of the impacted surface (e.g., microstructure and hardness), and the properties of the impacting particles (e.g., morphology, size, impact angle, velocity, and hardness) [2,11–14]. The erosion rate (ER), a crucial parameter for evaluating surface degradation, is defined as the rate at which material is removed from the surface, i.e., the mass or volume of material lost per unit of time or unit area. The key determinant is the angle at which particles strike a surface [15]. Ductile metals experience maximum ERs at low angles (20–30°) due to micro-cutting, while brittle materials experience peak ERs at near-normal impacts (90°), leading to crack formation and spallation. Particle characteristics, such as size, shape, and hardness, also critically influence erosion outcomes [16,17]. Another crucial factor influencing SPE is the velocity and, thus, the kinetic energy of the impacting

particles [18]. It has been observed that ER increases with particle size and kinetic energy up to a threshold, beyond which this relationship may become nonlinear due to particle-particle interactions [19,20].

Among the various weld overlay coating materials employed to counteract SPE (e.g., iron-based, cobalt-based, nickel-based, and copper-based alloys) [21], iron-based hardfacing materials are often favored [22–25]. This is largely attributed to their cost-effectiveness and performance characteristics. Notably, high chromium cast irons (HCCIs) are renowned for their excellent wear and corrosion resistance, which stem from their peculiar microstructure. They consist of hard primary and eutectic carbides (M_7C_3 or $M_{23}C_6$ types) embedded in a tough matrix. Broadly speaking, the primary carbides act as a barrier against erosion, whereas the surrounding matrix provides ductile support to the carbides.

As reported, SPE is a challenging phenomenon, and many investigations have explored specific aspects of the erosion phenomenon, focusing on individual parameters that influence erosive behavior. For instance, Sapate and Rama Rao [26,27], explored the relationship between carbide volume fraction (CVF) and ER under mild and severe erosion conditions, analyzing the protective role of carbides against softer erodents and the opposite effect in the presence of harder erodents. Chatterjee and Pal [22] analyzed the SPE of hardfacing deposits on gray cast iron, highlighting that CVF and carbide type significantly influence erosion resistance, with softer erodents causing less damage and hard erodents leading to severe wear in alloys with brittle carbides. Similarly, Stevenson and Hutchings [28] demonstrated that CVF is critical for erosion resistance, with results varying based on the relative hardness of the erodents. In parallel, the kinetic energy of impacting particles has been observed to play a fundamental role in intensifying erosion. As discussed by Finnie [29], who modeled the relationship between particle velocity and ER, higher kinetic energy amplifies surface damage. However, the effect of kinetic energy is often studied separately from microstructural considerations. Shitole et al. [30] investigated the influence of particle kinetic energy, varying with particle size, on SPE of metals. The findings suggested a direct correlation between increased kinetic energy and higher ERs, showing that higher-energy particles cause more severe material degradation.

In summary, while numerous studies have provided valuable insights into SPE, none, to the best of the author's knowledge, have comprehensively examined the combined effects of microstructural characteristics and the kinetic energy of impacting particles, often overlooking their complex interplay. The primary purpose of this study is to address this research gap by investigating how the microstructure of an HCCI interacts with particle kinetic energy to influence erosion resistance. Specifically, the study aims to determine why substrates with similar CVFs exhibit differing levels of damage under identical erosion conditions (i.e., the same particle kinetic energy), thereby advancing the understanding of structure-property relationships. To achieve this objective, a detailed microstructural analysis through optical and scanning electron microscopes was performed. The erosion tests, conducted in a dedicated test rig designed according to the guidelines outlined in the ASTM G76 standard [31], comprised a standard powder (ISO 12103-1 standard [32]) with different granulometric distributions. Tests were conducted at a 15° impact angle and by keeping kinetic energies constant. The findings reveal that substrates with the same CVFs can suffer different damage levels even when subjected to identical particle kinetic energies. This underscores the need for a quantitative approach to deepen our understanding of structure-property relationships, enhance microstructure design, and optimize processing methods. By providing new insights into the complex relationship between microstructure and erosion mechanics, this study advances the understanding of the erosion process and contributes to improving the design and durability of HCCIs for demanding applications.

2. Materials and Methods

In this study, a commercial hardfacing alloy was utilized, featuring an HCCI overlay applied on a low-carbon steel substrate. The overlay was deposited using an open-arc welding process with a flux-cored wire through commercial process parameters. The HCCI hardfacing electrodes were deposited onto a low-carbon steel plate, with the base steel and the hardfacing layer having a nominal thickness of 5 mm. To determine the chemical composition of the HCCI, Glow Discharge Optical Emission Spectroscopy (GDOES, Spectruma Analytik, Hof, Germany) was performed, and the result is summarized in Table 1.

Table 1. Chemical composition (wt.%) of the HCCI overlay.

Composition (wt.%)—Fe Balance							
C	**Mn**	**Si**	**Cr**	**Mo**	**Nb**	**W**	**V**
4.15	0.56	1.08	21.04	2.78	4.09	0.86	0.69

The microstructural analyses of the material were conducted using a Leica DMi8 A optical microscope (OM) (Leica, Wetzlar, Germany) and a Zeiss EVO MA15 (Carl Zeiss, Jena, Germany) scanning electron microscope (SEM), equipped with an Oxford X-Max 50 (Oxford Instruments, Abingdon-on-Thames, UK) Energy Dispersive Spectroscopy (EDS) X-ray microprobe for semi-quantitative analysis. SEM investigations comprised secondary electron (SEI) and backscattered electron (BSE) detectors. After standard metallographic preparation (up to 3 μm diamond polishing), the surface was etched with Kalling's reagent (5 g $CuCl_2$, 100 mL HCl, 100 mL C_2H_5OH). A detailed quantitative description of the microstructural features of the HCCI was conducted to deepen the role of the microstructure on the solid particle erosion phenomenon. The 20 mm × 20 mm (which represents the area of the target used in the erosion tests described hereafter) surface of each sample was divided into 9 regions of interest (ROIs), covering a total area of about 18 mm^2 per sample. Through ImageJ image analysis software (Version 1.53e, 2020, National Institutes of Health, Bethesda, MD, USA) [33], the stereological features of the Cr-rich carbides were determined. Figure 1 displays the sequence of the adopted image processing procedure. Figure 1a presents the original grayscale OM micrograph. The latter was converted into an 8-bit binary image, and contrast enhancement techniques were applied to facilitate feature extraction. By setting the threshold value for identifying the features under examination (specifically, the primary Cr-rich carbides), each particle was outlined, ensuring precise delineation of the carbides for accurate quantification. Figure 1b illustrates the outcome of particle analysis, where carbides below a specified area threshold were excluded, displaying only the outlines of the measured carbides. This selective exclusion was achieved by defining a minimum size threshold to filter out undesired carbides based on their area. This sequence was adopted to determine the CVF parameter, computed as the A_C/A_{TOT} ratio, where A represents the area, the subscripts C and TOT refer to carbides, and the total analyzed microstructure area.

Solid particle erosion tests were conducted per the ASTM G76 standard in an on-purpose bench. The bench has two main sections: the particle injection system and the impact test chamber. The particle injection system comprises a volumetric feeder that ensures a stable flow rate of erodent powder, which is calibrated for precise mass flow control by adjusting the motor speed via an inverter. Once dosed, the powder reaches a mixing chamber connected to the main airflow. Here, high shear forces generated by a Venturi nozzle prevent particle agglomeration, thus ensuring a consistent particle stream. The high-speed airflow carries the particles through the nozzle, where they are accelerated to the desired impact velocity. Nozzle geometry is optimized to guide the particle-laden

jet toward the target material with minimal dispersion. The specimen is placed in a target holder, which can be tilted to test different impact angles, i.e., from tangential (15°) to normal (90°) impacts. Figure 2 shows the test chamber. An exhaust fan coupled with a filtration system prevents particle dispersion outside the chamber. Further details regarding the test bench can be found in [34].

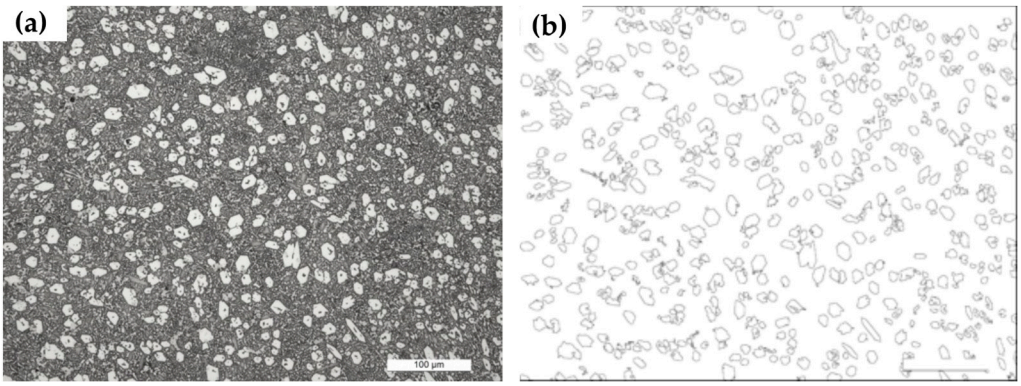

Figure 1. Sequence of the adopted image processing procedure with ImageJ image analysis software: (**a**) original grayscale OM micrograph and (**b**) outcome of particle analysis.

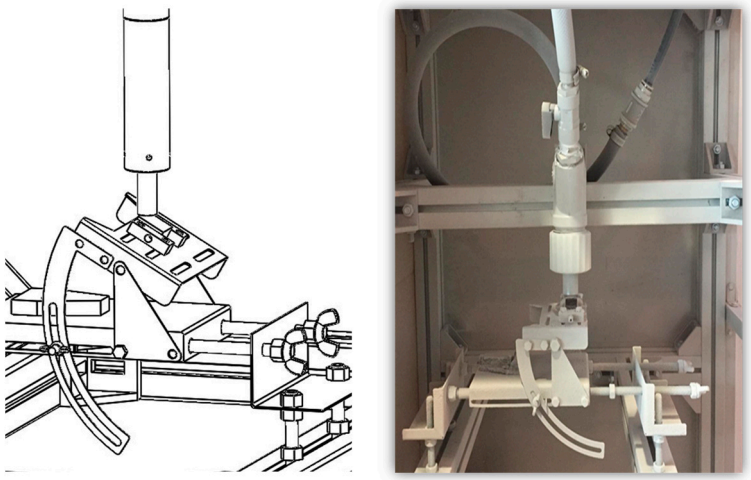

Figure 2. Scheme and image of the impact test chamber.

Tests were conducted on polished surfaces (3 µm diamond polishing) with an impact angle of 15°. The erodent powder selected was the controlled-grain-size standard Arizona dust quartz (ARD), in accordance with ISO 12103-1:2016. This commercial powder comprises 75% silica dioxide, 20% aluminum trioxide, and minor oxides (such as magnesium and iron) and is commonly used to test filtration systems and assess machine degradation. Two mean particle diameters of the ARD powder were chosen, specifically dmean = 4.8 µm (labeled as UF) and dmean = 25.5 µm (labeled as M). Test parameters, including flow rate, injected powder flow rate, and test duration, were established using computational fluid dynamics simulations to ensure a working condition with constant kinetic energy of the erodent particles. Hence, UF powder had an impact velocity of 205 m/s, whereas M powder had an impact velocity of 15.9 m/s. This difference in velocity compensates for the varying particle masses, ensuring that the tests were conducted under equivalent kinetic energy conditions. Erosion resistance was assessed by measuring the sample weight loss using a Kern ABT 100-5NM (Kern, Balingen, Germany) analytical balance with a resolution of 0.01 mg. The ER was computed as the ratio of sample weight loss to the mass of injected erodent, and ER values were averaged over five tests for each substrate-erodent combination.

On the worn surfaces, qualitative and quantitative analyses comprised observations using a HIROX-RH 2000 (Hirox Europe, Limonest, France) 3D digital microscope and using a Talysurf CCI-Lite (Taylor-Hobson, Leicester, UK) non-contact 3D profilometer, respectively.

3. Results and Discussion

Figure 3 shows the OM micrographs of the investigated HCCI, highlighting its main metallographic features. As seen, the microstructure is composed of primary carbides (i.e., the light phase in the micrographs) embedded in the surrounding matrix. Such a microstructure is in accordance with the chemical composition of the HCCI, and the as-welding morphology of M_7C_3 carbides of hypereutectic Fe-Cr-C alloy depends on the solidification rate [35]. Thus, some regions exhibit hexagon and hollow-hexagon morphologies of primary M_7C_3 carbides (see Figure 3a), whereas others display blade-like primary carbides (see Figure 3b). In addition to the morphologies, the distribution of the carbides differs since they appear relatively uniformly distributed in Figure 3a and form a star-like pattern emanating from nucleation centers in Figure 3b, as a result of directional solidification phenomena.

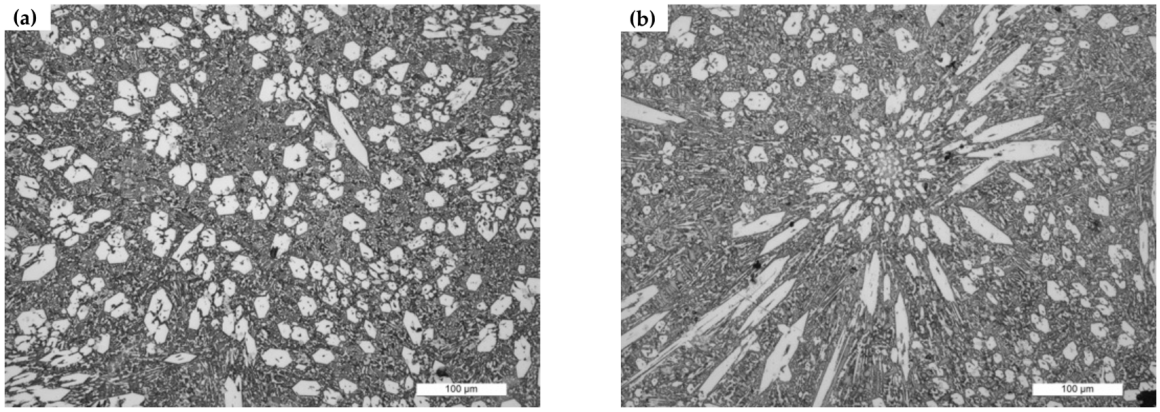

Figure 3. OM micrographs of the investigated HCCI: (**a**) hexagon and hollow-hexagon morphologies of primary M_7C_3 carbides; (**b**) blade-like morphology of primary M_7C_3 carbides.

The SEM analyses enabled us to attain more insight into the metallographic features of carbides and of the surrounding matrix. Figure 4a shows a low-magnification SEI-SEM micrograph representative of the HCCI microstructure. As seen, a large number of M_7C_3 carbides evenly distributed in the matrix are detectable, identifiable by their characteristic hexagonal shape. In addition, several eutectic carbides surrounding the primary ones are also visible (see the solid circles in Figure 4a). Such carbides are likely the M_6C-type ones, as previously observed in [36,37]. Given the Nb content in the alloy (see Table 1), the micrograph also revealed the presence of NbC with flower-like or polygonal shapes (see the dashed circles in Figure 4a). It has been established that the improvement of wear resistance by Nb addition depends on the very hard NbC (2400 HV) and on the dissolution of Nb in the matrix that promotes higher hardness [38–42]. From the high-magnification SEI- and BSE-SEM micrographs of Figure 4b,c additional microstructural features were detailed. The SEI-SEM micrographs of Figure 4b confirmed the presence of primary and eutectic carbides, Nb-rich carbides surrounded by an austenitic matrix with a small amount of martensite (see the arrows in Figure 4b). Readers seeking more in-depth insights on matrix microstructure and on the role of its structure in affecting SPE resistance are referred to a preceding study by the authors [43]. As previously observed [44], the local depletion of austenite from alloying addition promotes martensite formation at the matrix/carbide interface. In addition to the EDS point analyses of the M_7C_3 carbides (Figure 4d) and of the

NbC (Figure 4e), Figure 4f displays the spectrum of the detected Mo-rich carbides. Such carbides were also detected in a previous study by the authors [43] in which XRD analyses comprehensively detailed the phase compositions of the investigated HCCI. The formation of such hard carbides refines the primary M_7C_3 ones and improves the hardness and wear resistance of the material [40,45,46].

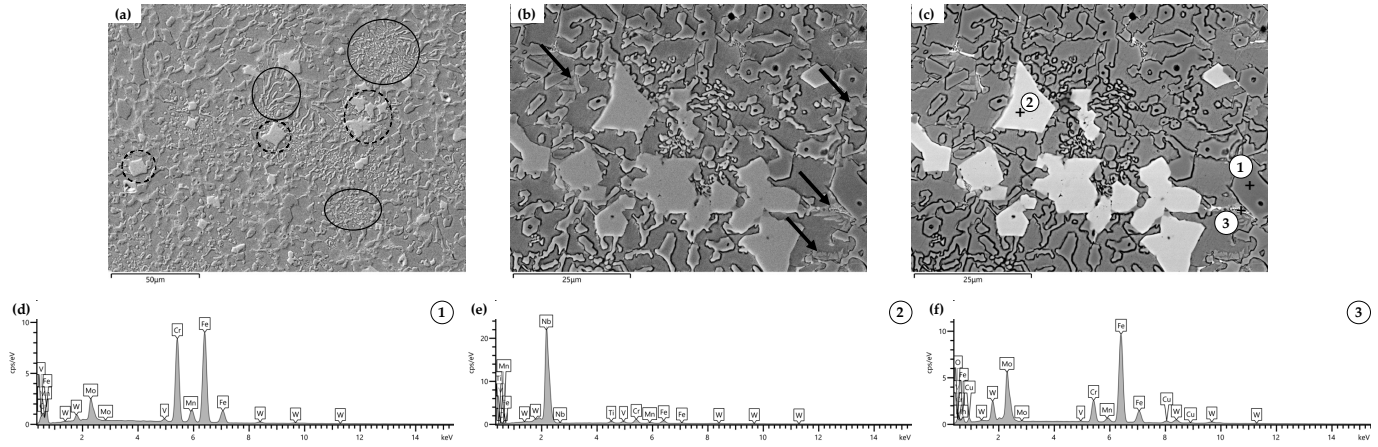

Figure 4. Micrographs of the investigated HCCI: (**a**) low-magnification SEI-SEM micrograph representative of the HCCI microstructure, eutectic carbides labeled with solid circles, and NbC labeled with dashed circles; (**b**) high-magnification SEI-SEM micrograph with martensite labeled with arrows (**c**) high-magnification BSE-SEM micrograph with labeled EDS point analyses; (**d**–**f**) EDS spectra of the point analyses labeled in (**c**).

The quantitative description of the microstructure was performed to further detail the carbide morphologies and their distribution within the microstructure. The qualitative and quantitative comparison among the different morphologies was considered, as reported in Figure 5, where the representative OM micrographs found within the microstructure of the investigated samples are shown. Table 2 reports the corresponding CVF parameters for each micrograph of Figure 5. As seen, according to the variations in carbide morphologies and dimensions, the CVF data vary from 0.14 up to 0.63 in the micrographs. It is worth noting that the adopted welding process is a commercial one, which inherently introduces variability in the microstructure due to local differences in solidification conditions. To provide context, the solidification of HCCI alloys is well understood in terms of equilibrium phase diagrams, as extensively discussed in the literature [47,48]. However, in commercial-grade materials, deviations from idealized solidification behavior are common due to the impact of real-world processing parameters, and understanding these deviations is essential for optimizing the performance of commercially manufactured components. Based on this experimental evidence, the CVF parameter was evaluated for both sample series tested with UF and M powders, respectively. The CVF was averaged on the surfaces of each sample series, i.e., covering a total area of about 54 mm^2. The results are collected in Table 3, which shows that the samples of the erosion tests had comparable CVF values. Such an outcome enables testing samples with comparable microstructure and, thus, only deals with the effect of particle dimension of the erodent powder.

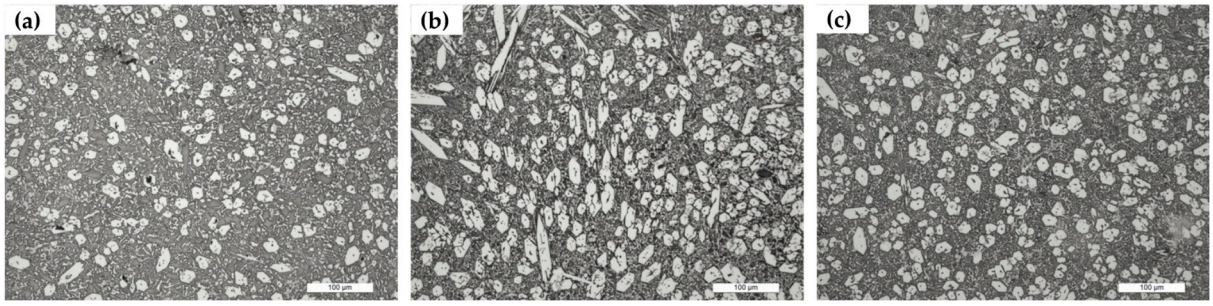

Figure 5. Representative OM micrographs of the varying morphology of primary carbides within the microstructure: (**a**–**c**) displays the variations in carbide morphologies and dimensions.

Table 2. CVF values of the representative OM micrographs in Figure 5.

Micrograph	CVF = A_C/A_{TOT}
a	0.14
b	0.63
c	0.42

Table 3. Erosion tests conditions and results: mean CVF values of the samples, kinetic energy, and ERs.

Sample Series	CVF = A_C/A_{TOT}	Kinetic Energy [J]	ER [μg/g]
UF	0.30 ± 0.14	6×10^{-8}	63.9
M	0.29 ± 0.12	2×10^{-7}	4.1

Table 3 also reports the condition (constant kinetic energy) and the obtained results (ERs) of the erosion tests. As seen, for the UF powder, the ER resulted in 63.9 μg/g, whereas for the M powder, the ER resulted in 4.1 μg/g. These outcomes highlighted that the CVF parameter is insufficient to account for the erosion resistance of the material. It is worth noting that by keeping the substrate characteristics (i.e., CVF), erodent powder type, and kinetic energy of the impacting particles constant, the result is 16 times greater ER for the UF powder. Based on these experimental findings, it emerges that for the investigated ARD-HCCI tribology coupling, the ER cannot be assessed according to the known literature models [2] where kinetic energy drives the magnitude of the damaging process.

To gain a deeper understanding of the wear damage that occurred, the worn surfaces were analyzed using a 3D digital microscope. Representative images, summarized in Figure 6, provide an overview of damage propagation across the matrix and carbides, effectively highlighting key differences in erosion behavior. From the comparison between the eroded surface of the HCCI exposed to ARD powder with a mean particle diameter of 4.8 μm (Figure 6a), i.e., UF powder, and with a mean particle diameter of 25.5 μm (Figure 6c), i.e., M powder, the difference in wear damage is evident. Consistent with the ERs data, the surface of Figure 6a exhibits remarkable wear damage with pronounced deformation features, including deep grooves. Such large-scale erosion marks suggest the particles' flow direction (from the top to the bottom in the image). By contrast, the surface morphology resulting from erosion by ARD powder with a mean particle diameter of 25.5 μm (Figure 6c) displays negligible deformation since the original microstructural features are still evident. Such outcomes are also confirmed by the high-magnification images reported in Figure 6b,d. The close-up of Figure 6b, which is a magnified view of the area depicted in Figure 6a, provides further evidence of the highly localized stresses upon impact, leading to material removal, confirming the severe abrasive wear mechanisms at play. The increased impact velocity of UF powder leads to more substantial

material displacement compared to the lower impact velocity associated with M powder, as seen by the comparison with the enlarged view of Figure 6d. This image highlights the smoother, eroded surface, suggesting a gradual material removal without significant plastic deformation due to the lower impact velocity.

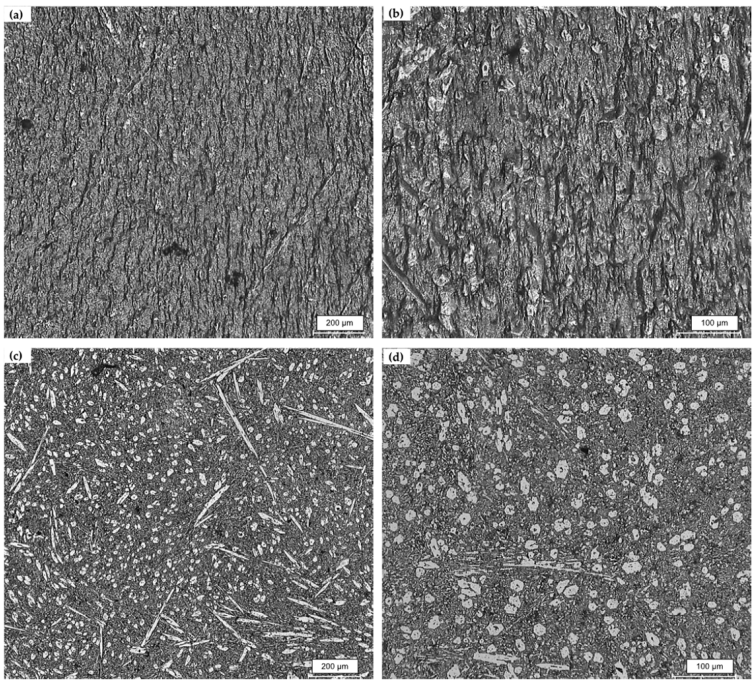

Figure 6. Digital microscope images of the worn surfaces: (**a**,**c**) low-magnification images of the surface eroded by ARD powder with a dmean = 4.8 µm and with a dmean = 25.5 µm, respectively; (**b**,**d**) high-magnification images of the surface eroded by ARD powder with a dmean = 4.8 µm and with a dmean = 25.5 µm, respectively.

Finally, the surface texture of the worn surfaces is compared in the 3D isometric views of Figure 7. As seen, these observations highlighted the contrasting erosion morphologies resulting from the different sizes and velocities of the erodent particles. The surface eroded by ARD powder with a dmean = 4.8 µm (Figure 7a) is more worn, as confirmed by the areal surface roughness parameter Sa, i.e., the arithmetical mean height. For Figure 7a, the Sa resulted in 2.24 ± 0.13 m, whereas for Figure 7b, it is 0.10 ± 0.02 µm. Hence, the smaller particles produce deeply grooved textures and pronounced ridges, indicating more aggressive material removal caused by the higher impact velocity that generated concentrated localized stresses upon impact. This leads to significant surface deformation, characterized by material displacement and detachment, and a rough topography marked by sharp peaks and valleys. Such morphology is consistent with the abrasive nature of high-velocity impacts, where the particles repeatedly erode the surface through mechanical wear. In contrast, larger impacting particles, moving at a lower velocity, produce smoother surfaces. The lower velocity reduces the severity of material removal. These contrasting morphologies highlight the critical role of erodent particle size and velocity in determining erosion mechanisms. Smaller particles at high velocities amplify surface roughness and material loss, while larger, slower particles predominantly cause negligible localized deformation, preserving much of the original surface integrity.

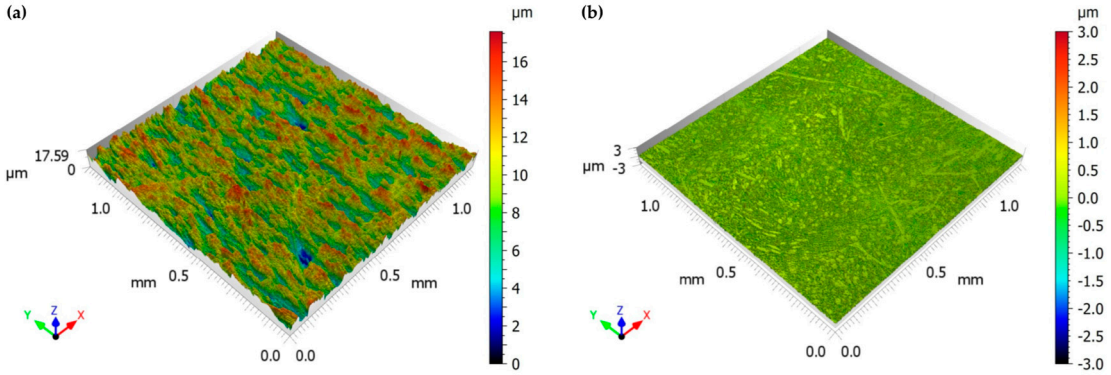

Figure 7. 3D isometric views of the worn surfaces eroded by ARD powder with: (**a**) dmean = 4.8 µm and (**b**) dmean = 25.5 µm.

4. Conclusions

This study analyzed the solid particle erosion resistance of a high chromium cast iron, focusing on the combined role of microstructural features and the kinetic energy of impacting particles. The following conclusions can be drawn based on the experimental outcomes resulting from both microstructural investigations and erosion tests.

- detailed quantitative microstructural analyses revealed that the CVF parameter was comparable across samples;
- erosion tests comprised two mean particle diameters of the ARD powder (dmean = 4.8 µm, labeled as UF, and dmean = 25.5 µm, labeled as M). Tests conducted at equal particle kinetic energy and CVF revealed varying damage levels in the substrates, highlighting that impact conditions, particularly velocity, outweigh the contribution of CVF alone. With UF powder, the HCCI substrate experienced markedly higher erosion rates (ER = 63.9 µg/g), characterized by severe surface damage and localized material removal. Conversely, M powder promoted lower erosion rates (ER = 4.1 µg/g) with minimal deformation;
- the erosion tests demonstrated a significant dependence of ER on the size and velocity of erodent particles, with smaller, faster particles causing more severe erosion (ER = 63.9 µg/g) due to their higher localized impact. Conversely, larger particles produced less pronounced wear (ER = 4.1 µg/g), inducing negligible deformation since the original microstructural features are still evident.

This study addresses critical gaps in the understanding of SPE behavior in HCCIs, providing valuable insights for optimizing the design and processing of HCCIs. The research sheds light on the interplay between carbide morphology, distribution, and SPE behavior, a partially underexplored area. By demonstrating how substrates with identical CVF exhibit varied erosion resistance due to differences in morphology and distribution, the study provides valuable insights for tailoring HCCI microstructures to enhance performance in demanding erosive environments.

Author Contributions: Conceptualization, A.S. and A.F.; methodology, A.S.; investigation, N.Z. and A.F.; data curation, A.F.; writing—original draft preparation, A.F.; writing—review and editing, A.S. and N.Z.; visualization, A.F. All authors have read and agreed to the published version of the manuscript.

Funding: This research received no external funding.

Data Availability Statement: The original contributions presented in this study are included in the article. Further inquiries can be directed to the corresponding author.

Acknowledgments: The authors wish to gratefully acknowledge Matteo Fucci for his support in the micrographic analyses. Our gratitude is also extended to Michele Gragnanini for his support with the non-contact 3D profilometer measurements.

Conflicts of Interest: The authors declare no conflicts of interest.

References

1. Budinski, K.G. Solid Particle Erosion. In *Friction, Wear, and Erosion Atlas*; CRC Press: Boca Raton, FL, USA, 2013; pp. 125–138.
2. Tarodiya, R.; Levy, A. Surface Erosion Due to Particle-Surface Interactions—A Review. *Powder Technol.* **2021**, *387*, 527–559. [CrossRef]
3. Ruff, A.W.; Wiederhorn, S.M. Erosion by Solid Particle Impact. In *Treatise on Materials Science and Technology*; Academic Press: Cambridge, MA, USA, 1979.
4. Kleis, I.; Kulu, P. *Solid Particle Erosion*; Springer: London, UK, 2008; ISBN 978-1-84800-028-5.
5. Fortini, A.; Suman, A.; Zanini, N. An Experimental and Numerical Study of the Solid Particle Erosion Damage in an Industrial Cement Large-Sized Fan. *Eng. Fail. Anal.* **2023**, *146*, 107058. [CrossRef]
6. Grant, G.; Tabakoff, W. Erosion Prediction in Turbomachinery Resulting from Environmental Solid Particles. *J. Aircr.* **1975**, *12*, 471–478. [CrossRef]
7. Alqallaf, J.; Ali, N.; Teixeira, J.A.; Addali, A. Solid Particle Erosion Behaviour and Protective Coatings for Gas Turbine Compressor Blades—A Review. *Processes* **2020**, *8*, 984. [CrossRef]
8. Parsi, M.; Najmi, K.; Najafifard, F.; Hassani, S.; McLaury, B.S.; Shirazi, S.A. A Comprehensive Review of Solid Particle Erosion Modeling for Oil and Gas Wells and Pipelines Applications. *J. Nat. Gas Sci. Eng.* **2014**, *21*, 850–873. [CrossRef]
9. Bousser, E.; Martinu, L.; Klemberg-Sapieha, J.E. Solid Particle Erosion Mechanisms of Protective Coatings for Aerospace Applications. *Surf. Coat. Technol.* **2014**, *257*, 165–181. [CrossRef]
10. Aldi, N.; Casari, N.; Pinelli, M.; Suman, A.; Vulpio, A.; Saccenti, P. Performance Modification of an Erosion-Damaged Large-Sized Centrifugal Fan. In *Volume 1: Aircraft Engine; Fans and Blowers; Marine; Wind Energy; Scholar Lecture*; American Society of Mechanical Engineers: Houston, TX, USA, 7 June 2021.
11. Liebhard, M.; Levy, A. The Effect of Erodent Particle Characteristics on the Erosion of Metals. *Wear* **1991**, *151*, 381–390. [CrossRef]
12. Ediriweera, M.; Chladek, J.; Ratnayake, C. Effect of Impact Angle, Exposure Time, and Particle Size on Impact Erosion. *Part. Sci. Technol.* **2021**, *39*, 10–18. [CrossRef]
13. Desale, G.R.; Paul, C.P.; Gandhi, B.K.; Jain, S.C. Erosion Wear Behavior of Laser Clad Surfaces of Low Carbon Austenitic Steel. *Wear* **2009**, *266*, 975–987. [CrossRef]
14. Nguyen, V.B.; Nguyen, Q.B.; Zhang, Y.W.; Lim, C.Y.H.; Khoo, B.C. Effect of Particle Size on Erosion Characteristics. *Wear* **2016**, *348–349*, 126–137. [CrossRef]
15. Oka, Y.I.; Okamura, K.; Yoshida, T. Practical Estimation of Erosion Damage Caused by Solid Particle Impact: Part 1: Effects of Impact Parameters on a Predictive Equation. *Wear* **2005**, *259*, 95–101. [CrossRef]
16. Abdian, K.; Eslami, A.; Ashrafizadeh, F.; Fadaeifard, F.; Yingxin, G.; Mendez, P.; Barnes, N. Solid Particles Erosion Performance of a Fe–Cr–C Chromium Carbide Overlay. *Metallogr. Microstruct. Anal.* **2023**, *12*, 1055–1061. [CrossRef]
17. Goodwin, J.E.; Sage, W.; Tilly, G.P. Study of Erosion by Solid Particles. *Proc. Inst. Mech. Eng.* **1969**, *184*, 279–292. [CrossRef]
18. Lindsley, B.A.; Marder, A.R. The Effect of Velocity on the Solid Particle Erosion Rate of Alloys. *Wear* **1999**, *225–229*, 510–516. [CrossRef]
19. Lin, F.Y.; Shao, H.S. Effect of Impact Velocity on Slurry Erosion and a New Design of a Slurry Erosion Tester. *Wear* **1991**, *143*, 231–240. [CrossRef]
20. Sapate, S.G.; RamaRao, A.V. Effect of Erodent Particle Hardness on Velocity Exponent in Erosion of Steels and Cast Irons. *Mater. Manuf. Process.* **2003**, *18*, 783–802. [CrossRef]
21. Badisch, E.; Roy, M. Hardfacing for Wear, Erosion and Abrasion. In *Surface Engineering for Enhanced Performance Against Wear*; Springer: Vienna, Austria, 2013; pp. 149–191.
22. Chatterjee, S.; Pal, T.K. Solid Particle Erosion Behaviour of Hardfacing Deposits on Cast Iron—Influence of Deposit Microstructure and Erodent Particles. *Wear* **2006**, *261*, 1069–1079. [CrossRef]
23. Jindal, C.; Singh Sidhu, B.; Kumar, P.; Singh Sidhu, H. Performance of Hardfaced/Heat Treated Materials under Solid Particle Erosion: A Systematic Literature Review. *Mater. Today Proc.* **2022**, *50*, 629–639. [CrossRef]
24. Singla, Y.K.; Maughan, M.R.; Arora, N.; Dwivedi, D.K. Enhancing the Wear Resistance of Iron-Based Alloys: A Comprehensive Review of Alloying Element Effects. *J. Manuf. Process.* **2024**, *120*, 135–160. [CrossRef]
25. Suman, A.; Fortini, A. Effects of Heat Treatment and Erosion Particle Size on Erosion Resistance of a Hypereutectic High-Chromium Cast Iron. *Coatings* **2024**, *14*, 66. [CrossRef]

26. Sapate, S.; Rama Rao, A. Effect of Carbide Volume Fraction on Erosive Wear Behaviour of Hardfacing Cast Irons. *Wear* **2004**, *256*, 774–786. [CrossRef]
27. Sapate, S.G.; RamaRao, A.V. Erosive Wear Behaviour of Weld Hardfacing High Chromium Cast Irons: Effect of Erodent Particles. *Tribol. Int.* **2006**, *39*, 206–212. [CrossRef]
28. Stevenson, A.N.J.; Hutchings, I.M. Wear of Hardfacing White Cast Irons by Solid Particle Erosion. *Wear* **1995**, *186*, 150–158. [CrossRef]
29. Finnie, I. Erosion of Surfaces by Solid Particles. *Wear* **1960**, *3*, 87–103. [CrossRef]
30. Shitole, P.P.; Gawande, S.H.; Desale, G.R.; Nandre, B.D. Effect of Impacting Particle Kinetic Energy on Slurry Erosion Wear. *J. Bio-Tribo-Corros.* **2015**, *1*, 29. [CrossRef]
31. *ASTM G76-18*; Standard Test Method for Conducting Erosion Tests by Solid Particle Impingement Using Gas Jets. ASTM International: West Conshohocken, PA, USA, 2018.
32. *ISO 12103-1:2016*; Road Vehicles—Test Contaminants for Filter Evaluation—Part 1: Arizona Test Dust. ISO: Geneva, Switzerland, 2016.
33. Schneider, C.A.; Rasband, W.S.; Eliceiri, K.W. NIH Image to ImageJ: 25 Years of Image Analysis. *Nat. Methods* **2012**, *9*, 671–675. [CrossRef]
34. Fortini, A.; Suman, A.; Vulpio, A.; Merlin, M.; Pinelli, M. Microstructural and Erosive Wear Characteristics of a High Chromium Cast Iron. *Coatings* **2021**, *11*, 490. [CrossRef]
35. Liu, S.; Zhou, Y.; Xing, X.; Wang, J.; Ren, X.; Yang, Q. Growth Characteristics of Primary M7C3 Carbide in Hypereutectic Fe-Cr-C Alloy. *Sci. Rep.* **2016**, *6*, 32941. [CrossRef] [PubMed]
36. Li, P.; Yang, Y.; Shen, D.; Gong, M.; Tian, C.; Tong, W. Mechanical Behavior and Microstructure of Hypereutectic High Chromium Cast Iron: The Combined Effects of Tungsten, Manganese and Molybdenum Additions. *J. Mater. Res. Technol.* **2020**, *9*, 5735–5748. [CrossRef]
37. Imurai, S.; Thanachayanont, C.; Pearce, J.T.H.; Tsuda, K.; Chairuangsri, T. Effects of W on Microstructure of As-Cast 28 Wt.%Cr–2.6 Wt.%C–(0–10)Wt.%W Irons. *Mater. Charact.* **2015**, *99*, 52–60. [CrossRef]
38. He-Xing, C.; Zhe-Chuan, C.; Jin-Cai, L.; Huai-Tao, L. Effect of Niobium on Wear Resistance of 15%Cr White Cast Iron. *Wear* **1993**, *166*, 197–201. [CrossRef]
39. Bedolla-Jacuinde, A. Microstructure of Vanadium-, Niobium- and Titanium-Alloyed High-Chromium White Cast Irons. *Int. J. Cast Met. Res.* **2001**, *13*, 343–361. [CrossRef]
40. Jain, A.-S.; Chang, H.; Tang, X.; Hinckley, B.; Zhang, M.-X. Refinement of Primary Carbides in Hypereutectic High-Chromium Cast Irons: A Review. *J. Mater. Sci.* **2021**, *56*, 999–1038. [CrossRef]
41. de Melo, I.N.R.; da Silva, A.E.; de Faria, F.G.; Pinheiro, I.P.; da Silva, L.R.; Paniago, R.M. Influence of Niobium Adding on the Microstructure and Abrasive Wear Resistance of a Heat-Treated High-Chromium Near-Eutectic Cast Iron Alloy. *Mater. Res.* **2022**, *25*, e20210562. [CrossRef]
42. Pourasiabi, H.; Gates, J.D. Effects of Niobium Macro-Additions to High Chromium White Cast Iron on Microstructure, Hardness and Abrasive Wear Behaviour. *Mater. Des.* **2021**, *212*, 110261. [CrossRef]
43. Fortini, A.; Suman, A.; Zanini, N.; Cruciani, G. Erosive Wear Behavior of High-Chromium Cast Iron: Combined Effect of Erodent Powders and Destabilization Heat Treatments. *Coatings* **2022**, *12*, 1218. [CrossRef]
44. Tabrett, C.; Sare, I. Effect of High Temperature and Sub-Ambient Treatments on the Matrix Structure and Abrasion Resistance of a High-Chromium White Iron. *Scr. Mater.* **1998**, *38*, 1747–1753. [CrossRef]
45. Scandian, C.; Boher, C.; de Mello, J.D.B.; Rézaï-Aria, F. Effect of Molybdenum and Chromium Contents in Sliding Wear of High-Chromium White Cast Iron: The Relationship between Microstructure and Wear. *Wear* **2009**, *267*, 401–408. [CrossRef]
46. Chung, R.J.; Tang, X.; Li, D.Y.; Hinckley, B.; Dolman, K. Microstructure Refinement of Hypereutectic High Cr Cast Irons Using Hard Carbide-Forming Elements for Improved Wear Resistance. *Wear* **2013**, *301*, 695–706. [CrossRef]
47. Lin, C.-M.; Chang, C.-M.; Chen, J.-H.; Hsieh, C.-C.; Wu, W. Microstructural Evolution of Hypoeutectic, Near-Eutectic, and Hypereutectic High-Carbon Cr-Based Hard-Facing Alloys. *Metall. Mater. Trans. A* **2009**, *40*, 1031–1038. [CrossRef]
48. Khvan, A.V.; Hallstedt, B.; Broeckmann, C. A Thermodynamic Evaluation of the Fe–Cr–C System. *Calphad* **2014**, *46*, 24–33. [CrossRef]